Inter-Metal Interaction with a Threshold Effect in NiCu Dual-Atom Catalysts for CO_2 Electroreduction

Dazhi Yao, Cheng Tang, Xing Zhi, Bernt Johannessen, Ashley Slattery, Shane Chern, and Shi-Zhang Qiao*

Dual-atom catalysts (DACs) have become an emerging platform to provide more flexible active sites for electrocatalytic reactions with multi-electron/proton transfer, such as the CO_2 reduction reaction (CRR). However, the introduction of asymmetric dual-atom sites causes complexity in structure, leaving an incomprehensive understanding of the inter-metal interaction and catalytic mechanism. Taking NiCu DACs as an example, herein, a more rational structural model is proposed, and the distance-dependent inter-metal interaction is investigated by combining theoretical simulations and experiments, including density functional theory computation, aberration-corrected transmission electron microscopy, synchrotron-based X-ray absorption fine structure, and Monte Carlo experiments. A distance threshold around 5.3 Å between adjacent $Ni-N_4$ and $Cu-N_4$ moieties is revealed to trigger effective electronic regulation and boost CRR performance on both selectivity and activity. A universal macro-descriptor rigorously correlating the inter-metal distance and intrinsic material features (e.g., metal loading and thickness) is established to guide the rational design and synthesis of advanced DACs. This study highlights the significance of identifying the inter-metal interaction in DACs, and helps bridge the gap between theoretical study and experimental synthesis of atomically dispersed catalysts with highly correlated active sites.

1. Introduction

Single-atom catalysts (SACs), that is, isolated metal atoms coordinated by neighboring sites on the host support, have attracted significant attentions in heterogeneous catalysis owing to unique structure and maximized atomic utilization of them.[1] Generally, SACs feature homonuclear metal sites and manifest enhanced electrocatalytic activity for various reactions, especially oxygen reduction reaction (ORR).[2] However, such site homogeneity with a single kind of active center significantly hinders their performance in complex reactions where the adsorption of multiple intermediates demands independent regulation.[3] Taking CO_2 reduction reaction (CRR) as an example, the adsorption energy scaling relationship between *CO and other carbon-bound species reveals that the key reduction intermediates, *COOH and *CHO, cannot be stabilized independently of *CO.[3a,4] Such scaling relations generally result in high overpotential and low catalytic efficiency, thus leaving unsatisfactory CRR reactivity and selectivity in practice.[3c,4b,5] Aiming at higher flexibility in optimizing active centers and intermediate adsorption, dual-atom catalysts (DACs) have been proposed to construct asymmetric bimetallic sites.[6] The incorporation of second heteronuclear metal sites induces more top/bridge sites, diverse absorption strength and modes, and synergistic effects via inter-metal interaction, enabling a new degree of freedom to break the linear scaling relations of different intermediates and thus improve the reaction activity and selectivity.[6c,7] Recent reports including NiFe,[8] ZnLn,[9] IrNi,[10] and IrFe[11] moieties highlight the unique advantages and effective applications of DACs in lowering the reaction barrier (overpotential) and accelerating the reaction kinetics for multi-step electrocatalytic reactions including ORR and CRR.[7a,12]

With the promising development of SACs from monometallic to multi-metallic systems, the chemical interaction between individual atoms has been revealed as a crucial factor to alter electronic structures and catalytic reactivity.[13] However, the role and mechanism of inter-metal interaction have yet to be understood. The crucial challenges include: 1) bottleneck in the precise and controllable synthesis of DACs with well-defined configurations, 2) difficulty in characterizing the

D. Yao, C. Tang, X. Zhi, S.-Z. Qiao
Centre for Materials in Energy and Catalysis
School of Chemical Engineering and Advanced Materials
The University of Adelaide
Adelaide, SA 5005, Australia
E-mail: s.qiao@adelaide.edu.au

B. Johannessen
Australia Synchrotron
Australian Nuclear Science and Technology Organisation (ANSTO)
800 Blackburn Rd, Clayton, VIC 3168, Australia

A. Slattery
Adelaide Microscopy
The University of Adelaide
Adelaide, SA 5005, Australia

S. Chern
Department of Mathematics and Statistics
Dalhousie University
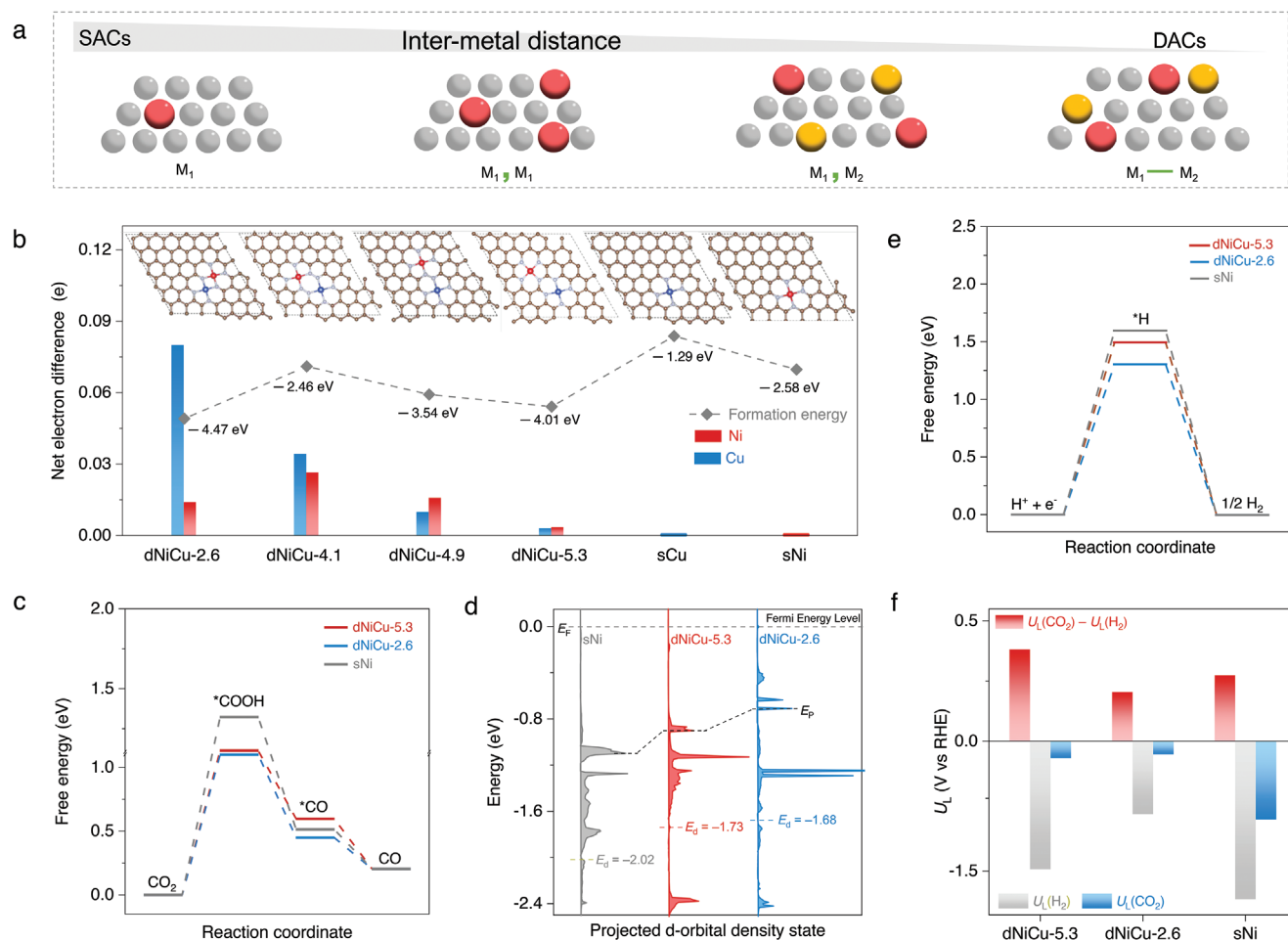Halifax, Nova Scotia B3H 4R2, Canada

Figure 1. Theoretical calculations to study the inter-metal interaction effect on the dNiCu model. a) Schematic of SACs and DACs showing the change in site proximity with different models. b) Net electron difference of Ni and Cu sites in different dNiCu models using sNi and sCu models as the baseline, respectively. c) Free energy diagrams of CO_2 electroreduction to CO on the Ni sites for dNiCu-5.3, dNiCu-2.6, and sNi models (U = 0 eV; pH = 6.8). d) Computed pDOS of the Ni d-orbital for dNiCu-5.3, dNiCu-2.6, and sNi models. e) Free energy diagrams of HER on the Ni sites for dNiCu-5.3, dNiCu-2.6, and sNi models (U = 0 eV; pH = 6.8). f) Calculated limiting potentials difference for CO_2 reduction over H_2 evolution on Ni sites.

adjacent and uniform distribution of heteronuclear atoms, and 3) knowledge gap between experimental observation and theoretical interpretation.[3a,14] Ideally, the heteronuclear metal sites in DACs are connected by linking or bridging atoms (e.g., O/N/S atoms) with a well-defined configuration on the host support (e.g., N-doped graphene), which is denoted as "M_1–M_2" in **Figure 1**a.[6b] However, such adjacent and specific moieties cannot be strictly and uniformly constructed by prevailing synthetic methods.[14,15] The simplified "M_1–M_2" model and corresponding atomic bonding/orbital coupling theory cannot rationalize the experimentally observed performance of DACs.[8b,15,16] As comparison, a new model of "M_1, M_2" for DACs which considers two crucial features, random distribution of heteronuclear metal sites and proximity effect between each other, is seldom studied.[3a,13a] The characteristics of "M_1, M_2" configuration can effectively bridge the research from isolated SACs (M_1) through correlated SACs (M_1, M_1) to ideal DACs (M_1–M_2) (Figure 1a), rendering a more justified and universal structure model to unravel the fundamental mechanism of inter-metal interaction.[6b] Therefore, it is urgent and crucial to first investigate the inter-metal distance (*d*) effect of DACs

based on the "M_1, M_2" configuration, which can not only promote the full potential of DACs, but also guide the design of advanced SACs with more flexibility in concentration, composition, structure, and property.

Herein, NiCu dual-atom dispersed on nitrogen-doped carbon (NiCu-NC) was selected as a case to investigate the inter-metal distance effect on its CRR performance. We first conducted theoretical predictions with various SACs and DACs models to evaluate the effect of inter-metal interaction on the electronic structure, and CRR activity and selectivity of DACs, revealing a distance threshold for effective inter-metal interaction. Further experimental synthesis, atomic characterization, and electrocatalytic measurement confirmed the superior CRR activity and selectivity of DACs over SACs, especially on the onset potential and CO selectivity. The non-bonding inter-metal interaction and synergistic effect were further elucidated by analyzing the electronic structure. Aiming at a more efficient and practicable design principle for DACs, we conducted random computational simulation and mathematical analysis to correlate the inter-metal distance with intrinsic material properties, such as the metal loading and substrate thickness. These findings offer

some fresh and qualitative insights into the structural understanding, activity origin, and rational design of DACs by regulating the inter-metal distance and synergistic effect.

2. Result and Discussion

2.1. Theoretical Investigation of Inter-Metal Interaction Effect

We first evaluated the inter-metal interaction of DACs and its effect on CRR performance by changing the inter-metal distance (d) between adjacent Cu and Ni atoms. As shown in Figure 1b, four DAC models were built with the same first coordination sphere configuration (metal−N_4) but varied d values for density functional theory (DFT) computation. The models are denoted as dNiCu-d, where d is calculated to be 2.6, 4.1, 4.9, and 5.3 Å, respectively. Two monometallic counterparts, donated as sNi and sCu, were also considered to simulate the DACs without inter-metal interaction by increasing d to infinity. All these DACs models are confirmed to be thermodynamically stable with lower formation energies than those of SACs (Figure 1b).

To investigate the effect of inter-metal interaction on electronic structures, we introduce the "net electron difference" ($|\Delta e|$) to reflect the d-dependent electron redistribution on both Ni and Cu sites. The $|\Delta e|$ value is set as zero for both sNi and sCu models as the baseline. As shown in Figure 1b, the DFT computation reveals a negative correlation between $|\Delta e|$ and d values for both sNi and sCu. The dNiCu-2.6 structure exhibits the most electron depletion on Cu (≈0.08 e) and some on Ni (≈0.02 e), and such electron redistribution effect is continuously weakened as the distance elongated. When d is larger than ≈5.0 Å, the electron difference is becoming negligible (<0.003 e) compared to that of sNi and sCu. Therefore, there is a distance threshold (here 5.3 Å) to trigger effective inter-metal interaction in terms of the electronic structures for DACs, which is consistent with the findings in densely populated Fe SACs.[13a] When d is closer than the threshold, the electronic structure of metal centers will be substantially altered by decreasing the inter-metal distance; however, the d-dependent effect will be negligible for the distance above the threshold. This two-stage d-dependent electronic interaction is believed to play a vital role in regulating the CRR activity and selectivity for DACs.

The influence of inter-metal interaction on CRR activity and selectivity was further studied by computing the free energy diagrams and limiting potentials (U_L) for different structures. We investigated the CO_2 reduction to CO through *COOH on both DACs (i.e., dNiCu-2.6 and dNiCu-5.3) and SACs (sNi, sCu). As shown in Figure 1c and Figure S1, Supporting Information, the formation of *COOH from CO_2 is the potential-limiting step for all cases, and the Gibbs free energy change of this step (ΔG_{COOH}) is used as the activity descriptor (Tables S1 and S2, Supporting Information). For all studied models, Ni sites are revealed to serve as the catalytic active centers with theoretical overpotentials relatively lower than those on Cu sites (Figure 1c and Figure S1, Supporting Information). Additionally, the formation of DACs facilitates the adsorption of *COOH, evidenced by the lower ΔG_{COOH} on the dNiNi-2.6 comparing with

sNi (Figure S1, Supporting Information). Compared to the SACs without inter-metal interaction, the dNiCu-5.3 moiety exhibits obviously decreased energy barrier (ΔG_{COOH}) and thus higher CRR activity on the Ni sites. Such enhancement effect by introducing a neighboring Cu site to Ni sites is further elucidated by investigating Ni 3d electronic configuration (Figure 1d and Figure S2, Supporting Information). As shown in Figure 1d, the computed partial density of states reveal an obvious upshift of the peak location (E_p, first maximum near Fermi energy) and d-band center (E_d) upon the incorporation of heterogeneous Cu sites and a decrease of the inter-metal distance. This regulated electronic structure is responsible for accelerated adsorption of reaction intermediates.[13b,17] Notably, the closer d will simultaneously strengthen the adsorption of *H for competing hydrogen evolution reaction (HER) on Ni sites (Figure 1e), resulting in a trade-off between CRR activity and selectivity. The limiting potentials for CRR over HER, that is, ($U_L(CO_2)−U_L(H_2)$), were applied as a reasonable descriptor to clearly figure out the CRR selectivity on the d-dependent Ni sites.[18] As compared in Figure 1f and Figure S3, Supporting Information, dNiCu-5.3 exhibits both high activity and selectivity for CRR, while dNiCu-2.6 is unfavorable due to the significantly decreased selectivity, even lower than that of Ni SACs.

The theoretical study well reveals that the electronic structure, CRR activity, and selectivity of DACs can be effectively altered by the inter-metal interaction, which is determined by the inter-metal distance. It is noteworthy that the d-dependence features a novel threshold effect. Specifically, for dNiCu-5.3 DACs featuring the threshold d, the inter-metal interaction-derived electronic structure regulation (<0.003 e) significantly promotes the *COOH adsorption for CRR (Figure 1c) while slightly improves the *H adsorption for HER on Ni sites (Figure 1e), thus rendering a highly active and selective catalyst for CO_2 reduction to CO. By further decreasing d, however, the strong electronic interaction (e.g., one order of magnitude higher for dNiCu-2.6) leads to unfavorable enhancement of HER and lower selectivity toward CRR (Figure 1e,f). Therefore, these theoretical findings highlight the crucial importance to refine the fundamental mechanism understanding of d-dependent synergistic effects to guide the design of DACs with optimal structures and properties.

2.2. Synthesis and Characterization of NiCu DACs

Guided by theoretical predictions, we synthesized peripherally dispersed NiCu DACs on the nitrogen-doped graphene (denoted as NiCu-NC) by pyrolyzing a mixture of dicyandiamide, glucose, nickel, and copper salts in the argon atmosphere (Figure S4, Supporting Information). Ni and Cu SACs, denoted as Ni-NC and Cu-NC, were also fabricated via similar approaches with the only addition of one corresponding salt precursor. Transmission electron microscopy (TEM) images show that the as-obtained NiCu-NC sample exhibits corrugated nanosheets with a multilayer thickness (**Figure 2**a,b). Such nanosheet morphology is attributed to the added dicyandiamide as a sacrificial template, which initially assembles into the layered graphitic carbon nitride (g-C_3N_4), and binds aromatic carbon intermediates from the glucose. Finally, graphene nanosheet is formed
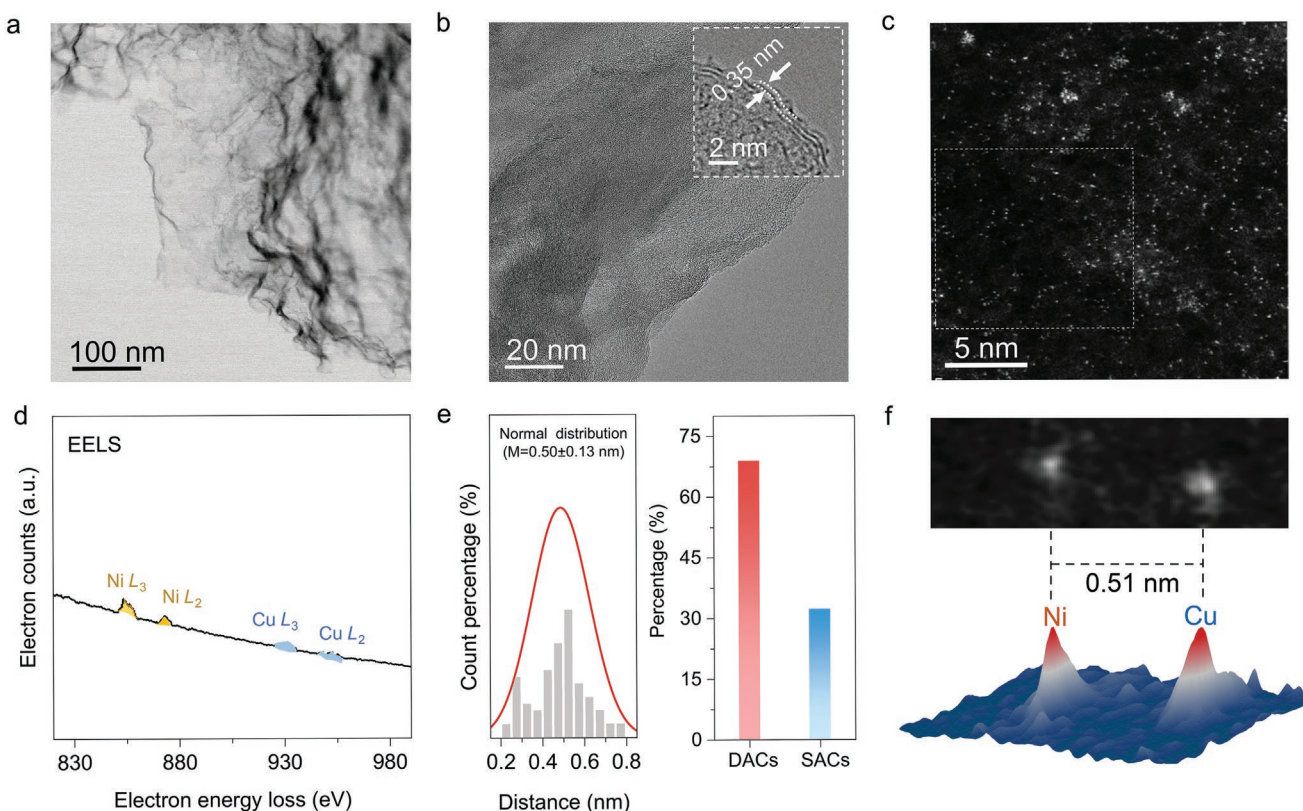
Figure 2. Atomic characterization of the obtained NiCu-NC DACs. a) TEM image and b) high-resolution TEM images of the as-obtained NiCu-NC. The insert in (b) shows the edge thickness of the N-doped carbon nanosheet. c) Representative atomic-resolution HAADF-STEM image and d) EELS of NiCu-NC. e) Histogram of the observed inter-metal distance (left) and percentage of DACs versus SACs with 5.3 Å as the threshold (right). f) Magnified HAADF-STEM image of a NiCu atomic pair and the corresponding 3D intensity profile.

at higher temperatures (900 °C) after the complete pyrolysis of g-C_3N_4.[19] The interplanar spacing (0.35 nm) is slightly larger than that of pristine multilayer graphene (0.335 nm), which might ascribe to the corrugation-derived lattice distortion and heteroatom-doped defects.[19b] Raman spectra further confirm the defective structure of nitrogen-doped graphene substrates, showing a large intensity ratio of D and G bands around 1.0 (Figure S5, Supporting Information). Such defective laminated morphology is beneficial for the uniform anchoring and dispersion of atomic metal species. Powder X-ray diffraction (XRD) analysis of as-obtained samples reveals two broad peaks centered around 28° and 44°, assigned to the (002) and (101) facets of graphitic carbon (Figure S6, Supporting Information).[20] The absence of diffraction peaks for metallic nanoparticles, as well as no pronounced agglomeration in high-resolution TEM images, suggests the formation of isolated Ni and Cu sites. As comparison, Ni-NC and Cu-NC samples were also characterized by Raman spectra, XRD spectra, and TEM images (Figures S5–S7, Supporting Information), both of which display identical features as NiCu-NC.

The atomic dispersion and inter-metal distance were further investigated by aberration-corrected high-angle annular dark-field scanning transmission electron microscopy (HAADF-STEM). The HAADF-STEM image of NiCu-NC DACs displays a large amount of well-dispersed, bright dots with different brightness and size below 2 Å on the carbon matrix (Figure 2c

and Figure S8, Supporting Information). They are assigned to isolated Ni and Cu metal atoms due to the atomic number-dependent contrast variation. Electron energy loss spectroscopy (EELS) and energy-dispersive X-ray spectroscopy mapping validate the uniform dispersion of Ni and Cu elements on the N-doped carbon matrix (Figure 2d and Figure S9, Supporting Information). CO adsorption measurement via in situ diffuse reflectance infrared Fourier transform (DRIFT) spectroscopy also verifies the formation of SACs.[21] As shown in Figure S10, Supporting Information, time-dependent DRIFT spectra reveal that CO absorption bands on NiCu-NC are centered at 2120 cm^{-1}. As the time of CO purging increases, the intensity of CO adsorption bands also increases. The uniform and isolated dispersion of metal atoms is also confirmed for Ni-NC and Cu-NC SACs samples (Figure S7, Supporting Information). The Ni and Cu metal loadings in NiCu-NC are quantified by inductively coupled plasma mass spectrometer (ICP-MS) to be ≈0.67 and 0.88 wt%, respectively. All the as-obtained DACs and SACs samples exhibit a similar total metal loading, ranging from 1.14 to 1.55 wt% (Figure S11 and Table S3, Supporting Information). These results further validate the atomic-resolution HAADF-STEM analyses, demonstrating the successful preparation of atomically dispersed NiCu-NC catalysts.

To gain more insights into the adjacent distribution of Ni and Cu atoms, we conducted statistical analysis by considering more than 300 atoms in HAADF-STEM images (Figure 2c and

Figures S8 and S12, Supporting Information). For one specific single-atom site, its inter-metal distance was determined by measuring the distance from its nearest metal site (Figure S12b, Supporting Information). As shown in Figure 2e, the statistic histogram of inter-metal distance satisfies a normal distribution, with a fitted average value of 0.50 ± 0.13 nm. If we take the theoretically predicted d value with effective inter-metal interaction (i.e., <5.3 Å) as the threshold between SACs and DACs, more than 60% of the bright single-atom dots can be regarded as bimetallic pairs (Figure 2e), which is comparable with and even higher than previous reports.[6d] Considering the great challenge to identify each metal atom by HAADF-STEM, this statistical analysis provides an effective, reasonable, and qualitative approach to investigating the inter-metal distance interaction in both DACs and densely populated SACs. Figure 2f exhibits the HAADF-STEM image and corresponding intensity profile for a typical NiCu bimetallic pair with different contrast and d of 0.51 nm. The atomic-resolution elemental analysis via EELS line-scan[8a,c] further corroborates the dual-atom element composition, that is, one Ni atom and one Cu atom with a diatomic distance of 5.1 Å (Figure S13, Supporting Information), which accounts for the largest proportion (Figure 2e) and matches well with the dNiCu-5.3 moiety.

2.3. Electronic and Coordination Structure Analysis of NiCu DACs

To identify the atomic structure and inter-metal interaction of as-obtained NiCu-NC DACs, we performed the synchrotron-based X-ray absorption fine structure (XAFS) spectroscopy characterization. As shown in **Figure 3**a, the Ni K-edge X-ray absorption near edge structure (XANES) spectra of NiCu-NC and Ni-NC locate between those of nickel (II) phthalocyanine (NiPc) and Ni Foil. It implies that the average valence state of isolated Ni atoms is between 0 and +2 in both SACs and DACs, which is the same for isolated Cu atoms (Figure 3b). The subtle difference in valence states between SACs and DACs is then investigated by the first-derivative XANES spectra (Figure 3c,d). Notably, the adsorption edges corresponding to the 1s → 4p transition[10,13b,22a] are almost identical (shift within 0.2 eV) for Ni K-edge between NiCu-NC (8338.3 eV) and Ni-NC (8338.1 eV) and for Cu K-edge between NiCu-NC (8981.6 eV) and Cu-NC (8981.5 eV), respectively. To further clarify the electronic states of Ni and Cu, we investigated the near-edge X-ray absorption fine structure (NEXAFS) spectrum for NiCu-NC. As shown in Figure S14, Supporting Information, the NEXAFS spectrum of N K-edge for NiCu-NC suggests an evident absorption at ≈399.5 eV, further proving the formation of metal−nitrogen bonding.[8a,22] The Ni L-edge of both NiCu-NC and Ni-NC shows a shoulder peak around 853.6 eV at the L_3 region, implying that Ni is partially oxidized state in both samples (Figure S14b, Supporting Information).[8a,10a] Also, no pronounced peak shift between NiCu-NC and Ni-NC further denotes the subtle interaction between atomical Ni and Cu sites, which is similar to that in the Cu L-edge of both NiCu-NC and Cu-NC (Figure S14c, Supporting Information). These findings reveal a subtle electronic structure change between as-obtained DACs and SACs, which is in line with the computation results of dNiCu-5.3 (Figure 1b) but different from previous reports.[13b,22]

To further investigate the coordination configuration of Ni and Cu atoms in NiCu-NC DACs and SAC counterparts, the extended X-ray absorption fine structure (EXAFS) was analyzed. Figure 3e,f displays the Fourier transform (FT) of k^3-weighted EXAFS spectra for Ni and Cu K-edge in the R-space, respectively. The Ni K-edge spectra exhibit a predominant peak around 1.45 Å for NiCu-NC and Ni-NC samples, similar to that for NiPc, which is assigned to the scattering of the first shell Ni−N path. The Cu K-edge spectra also feature the main peak around 1.5 Å originating from the Cu−N scattering for NiCu-NC and Cu-NC samples, in line with that for CuPc. Compared to Ni and Cu foils, the absence of metal−metal coordination (≈2.2 Å) for as-obtained DACs and SACs samples further corroborates the isolated dispersion of each metal and suggests a moderate distance without direct bonding between metal atoms. We also introduced wavelet-transform (WT) analysis for EXAFS spectra to identify the surrounding coordination of Ni and Cu centers in the radial distance and the k space.[23,24] As shown in Figure S15, Supporting Information, the maximum intensity of Ni K-edge and Cu K-edge spectra is found at ≈3.5 Å^{-1} for both NiCu-NC, Ni-NC and Cu-NC, which is attributed to the Ni−N or Cu−N scattering paths in the first coordination shell, consistent with FT-EXAFS results. At high radial magnitude (>2.5 Å), the WT-EXAFS intensity for NiCu-NC is comparable to these of Ni-NC and Cu-NC, but different from that of Ni/Cu metal foil.[10,22,23] Furthermore, the local coordination structure of NiCu-NC DACs was quantitatively analyzed by the least-squares EXAFS curve fitting using structure models with varied d values.[8b,23,24] The detailed fitting results, including metal−N/metal−metal path length and coordination numbers, are shown in Table S4, Supporting Information. If the sCu/sNi models with an infinitely large d or the dNiCu-2.6 model with a very small d are applied, the fitting curves exhibit significant deviation in the region of the second shell (Figures S16 and S17, Supporting Information). In contrast, the EXAFS curve fitting using the dNiCu-5.3 model achieves the best fitting coefficient and matches well with the experimental spectra for NiCu-NC (Figure 3g–i and Figures S18 and S19, Supporting Information). On one hand, the fitting results confirm an average coordination number of 4 for both Ni and Cu centers to form the Ni−N$_4$ and Cu−N$_4$ moieties in the first shell and eliminate the existence of Ni−Cu coordination bonds. On the other hand, additional metal−C/N bonds with longer lengths (>2.5 Å) have been found (i.e., Ni−C(16)/C(31) and Ni−N(1)/N(5) bonds in Table S4, Supporting Information), corroborating the non-bonding diatomic entity without direct metal−metal or metal−C/N−metal bonds. Taken together, the abovementioned characterizations of as-obtained NiCu-NC DACs, especially the HAADF-STEM and EXAFS results, match well with the proposed dNiCu-5.3 model in terms of the electronic structure change, local coordination configuration, and inter-metal distance.

2.4. CRR Activity and Selectivity of NiCu DACs

To investigate the electrocatalytic performance enhancement of DACs by inter-metal interaction, we conducted CRR measurements in CO_2-saturated 0.10 M KHCO$_3$ using a gas-tight

2209386 (5 of 10)

**ADVANCED
SCIENCE NEWS**

www.advancedsciencenews.com

**ADVANCED
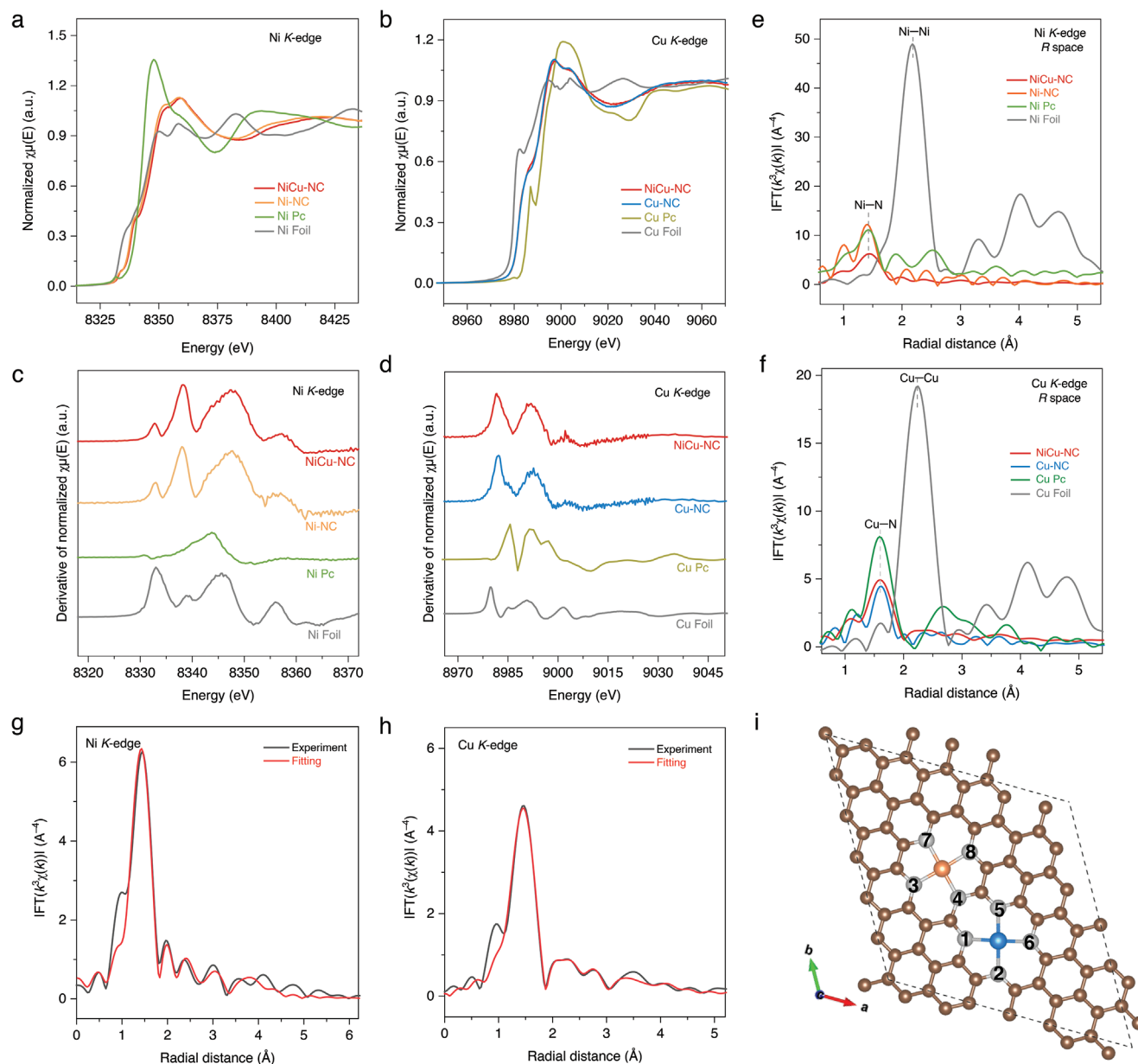MATERIALS**

www.advmat.de

Figure 3. Coordination structure analysis of the obtained NiCu-NC DACs. a) Ni K-edge and b) Cu K-edge XANES spectra. c) The derivative of the normalized Ni K-edge and d) Cu K-edge XANES spectra of NiCu-NC, Ni-NC, Ni/Cu Pc, and Ni/Cu foil. e) Ni K-edge and f) Cu K-edge FT-EXAFS spectra of different samples in R-space. g) The R-space EXAFS-fitting curves of the as-obtained NiCu-NC sample at Ni K-edge and h) Cu K-edge using the dNiCu-5.3 model. i) The most likely structural model of the as-obtained NiCu-NC. The brown, grey, orange, and blue balls represent C, N, Ni, and Cu atoms, respectively.

H-cell, which could provide much smaller biases and interference on the catalysts, thus leading to the slightest change in the structure of catalysts and benefit the clear mechanistic studies.[25] As shown in **Figure 4**a, the linear scan voltammogram tests reveal that NiCu-NC DACs deliver higher current responses than Ni-NC and Cu-NC SACs below −0.40 V vs reversible hydrogen electrode (RHE) in the CO_2-saturated electrolyte, implying its superior CRR activity. CRR selectivity was evaluated by chronoamperometry tests at different potentials (Figure S20, Supporting Information), and gaseous products were quantitatively analyzed by online gas chromatography.

CO and H_2 are identified as the predominant products over the whole potential range, with a total Faradaic efficiency (FE) close to 100% (Figure 4b,c). At an applied potential as positive as −0.32 V versus RHE, CO product can be obviously detected for NiCu-NC but is not evident for Ni-NC and Cu-NC samples, suggesting a smaller onset overpotential (η) of converting CO_2 to CO (Figure 4b). NiCu-NC sample can achieve a maximum FE for CO production (FE_{CO}) as high as ≈98%, much better than that of Ni-NC and Cu-NC SACs. Furthermore, NiCu-NC exhibits a significantly wide potential window for FE_{CO} >80% (from −0.47 to −1.27 V vs RHE; 800 mV), which is
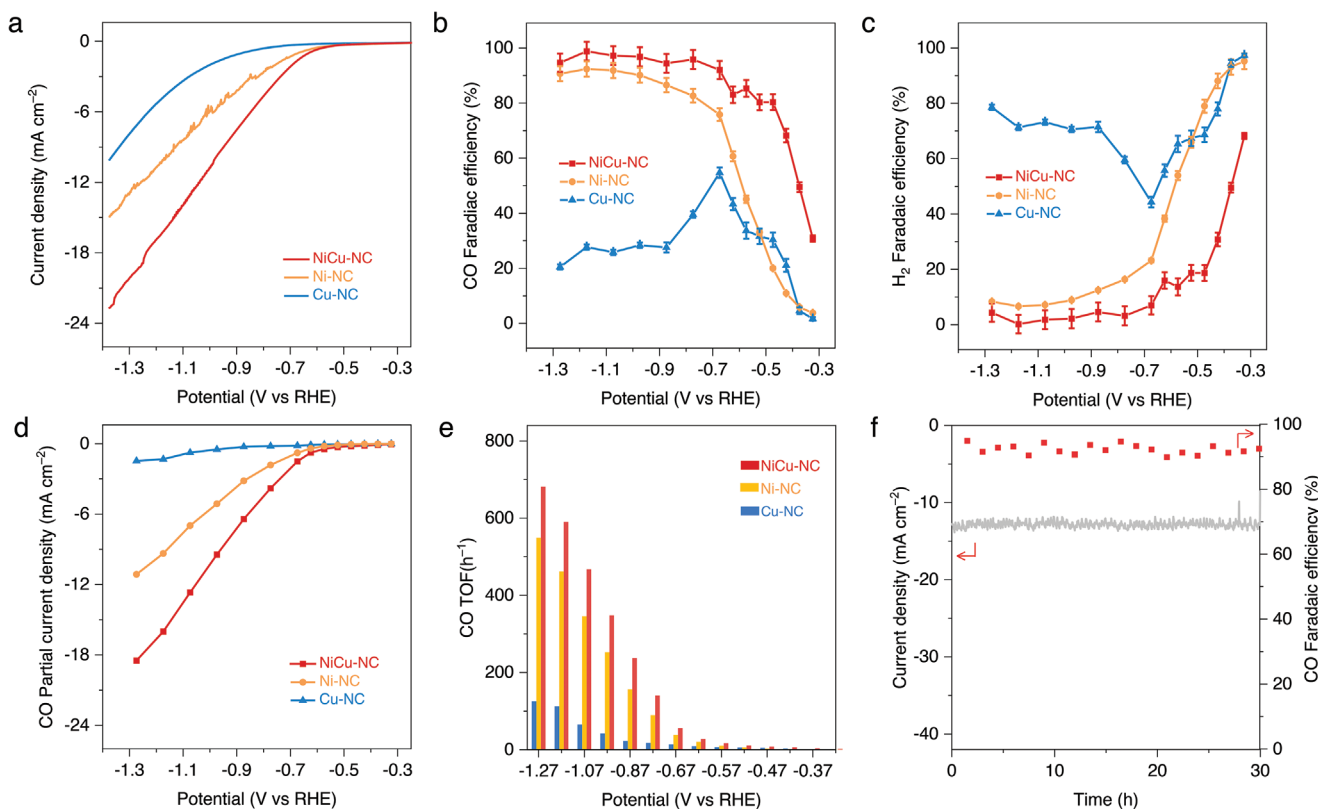
Figure 4. Catalytic performance of CO_2 electroreduction to CO. a) LSV polarization curves for NiCu-NC, Ni-NC, and Cu-NC in CO_2-saturated 0.1 M $KHCO_3$ electrolyte. b,c) Potential-dependent Faradaic efficiencies of CO (b) and H_2 (c) for NiCu-NC, Ni-NC, and Cu-NC in CO_2-saturated 0.1 M $KHCO_3$. The error bars were calculated by three independent tests. d) Potential-dependent CO partial current densities for different samples. e) Calculated TOF for NiCu-NC, Ni-NC, and Cu-NC on different applied potentials. f) Stability evaluation of NiCu-NC by chronoamperometric test at −1.07 V versus RHE for continuous 30 h.

≈200 mV wider than that of Ni-NC. Given the boosted activity and selectivity, NiCu-NC exhibits much higher CO partial current density (j_{CO}) over the entire potential window. Specifically, NiCu-NC can deliver a high j_{CO} of −18.2 mA cm^{-2} at −1.27 V versus RHE, which is ≈1.5 and ≈9 times greater than those of Ni-NC and Cu-NC, respectively (Figure 4d). Such CO_2-to-CO activity and selectivity of NiCu-NC are among the best results for state-of-the-art DACs and SACs evaluated in H-cells (Table S5, Supporting Information).

The superior intrinsic activity of NiCu-NC DACs is further illustrated by calculating the turnover frequency (TOF) for CO production based on the number of all metal sites (Ni and/or Cu), as well as the kinetics studies. As shown in Figure 4e, NiCu-NC exhibits a maximum TOF of 681 h^{-1} at −1.27 V versus RHE, which is ≈1.2 and ≈5.5 times higher than those of Ni-NC and Cu-NC, respectively. Moreover, NiCu-NC shows excellent durability for CRR electrocatalysis, demonstrated by the stable current density and FE_{CO} over 30 h during the continuous electrolysis at a constant potential of −1.07 V versus RHE (Figure 4f). Post-mortem microscopy characterization of NiCu-NC after long-term electrolysis indicates no formation of nanoparticles or nanoclusters by potential-induced agglomeration (Figure S21, Supporting Information). Additionally, we conducted Tafel analysis to understand the reaction kinetics of the NiCu-NC for the boosted catalytic performance. As shown in Figure S22, Supporting Information, the Tafel slope

for CO evolution on NiCu-NC is 138 mV dec^{-1}, where the first electron transfer can be attributed to a rate-determining step (RDS), that is, CO_2 activation with proton-coupled electron transfer (PCET).[26] The reaction order analysis elaborates more on the RDS (Figure S22b, Supporting Information). The approximate zero-order dependency on [HCO_3^-] suggests that the source of the proton in PCET step was mainly from water dissociation rather than directly from bicarbonate, that is, $* + CO_2 + H_2O + e^- = *COOH + OH^-$.[26] Compared with Ni-NC (257 mV dec^{-1}) and Cu-NC (289 mV dec^{-1}), NiCu-NC has the smallest Tafel slope, confirming its improved kinetics for the CO_2 to CO conversion, benefiting from the synergistic Ni/Cu dual sites. Such results are also consistent with the findings and rationality in the DFT computations, where sCu exhibited higher ΔG_{COOH} while the sNi or Ni site of the dNiCu-5.3 lowered the energy barrier (Figure S2, Supporting Information). These results manifest the crucial role of inter-metal interaction and synergistic effect between Ni and Cu atoms on enhancing the electrocatalytic performance of DACs, which will be elucidated further by theoretical studies. Since Ni sites are identified as the catalytic active centers (Figure 1 and Figure S2, Supporting Information), we analyzed the electron state change of Ni sites with *COOH bonded to investigate the synergistic mechanism in DACs. As compared in Figures S23 and S24, Supporting Information, upon *COOH adsorption on the Ni sites of dNiCu-5.3 and sNi, different electron transfer behaviors are

observed. For dNiCu-5.3, more electron depletion is observed on both Ni (from +1.03 to +1.16) and Cu sites (from +0.91 to +1.05). This synergistic interaction leads to 0.33e accumulation on the *COOH adsorbed onto the Ni site in the dNiCu-5.3, while COOH on the sNi can just receive 0.26e (Figure S23, Supporting Information), which can rationalize the similar net electron change but counterintuitively lowered *COOH adsorption energy between dNiCu-5.3 and sNi. Given the large inter-metal distance exceeding the metal−metal bond length, the electron contribution from Cu sites should be shuttled through the NC substrate to Ni sites, and finally to the *COOH intermediate. Therefore, such through-structure electron transfer is likely to be the active origin of the non-bonding synergistic interaction between neighboring DACs.

2.5. Macro-Descriptor for Rational Design of DACs

Although theoretical and experimental studies mutually verify the effect of inter-metal interaction and d-dependent electrocatalytic performance for DACs, it remains difficult to rationally design and synthesize DACs with favorable inter-metal interaction. Based on current technological advances on DACs synthesis, it is very reasonable to assume that the experimentally obtained DACs feature random distribution of metal atoms for most cases. The atomic distribution and inter-metal distance of metal sites can be mathematically analyzed by Monte Carlo experiments. Specifically, we built a 20 nm × 20 nm grid to stand for the N-doped graphene substrate, and randomly spread a certain amount of orange and blue spheres (radius: 0.15 nm, in equal numbers) inside to represent Ni atoms and Cu atoms in the NiCu-NC DACs. The distance between any given orange sphere and its nearest blue sphere was defined as the inter-sphere (i.e., inter-metal) distance (**Figure 5**a and Experimental Section). The random algorithm programming logic and details can be found in the Experimental Section. Figure 5a and Figure S25, Supporting Information, display the typical position distribution after randomly dispatching spheres with number ranging from 100 to 1200. It is noticeable that the range of inter-sphere distance decreases as the surface density of spheres (i.e., n = sphere number/grid area) grows (Figure 5b). When n increases from 0.25 to 3.0 nm^{-2}, the most probable inter-sphere distance will decrease from 1.11 to 0.29 nm (Figure 5c), which matches well with the d range for dNiCu-2.6 and dNiCu-5.3 moieties. Furthermore, by referring to a previously reported mathematical model investigating the distance between two random uniform points in a unit square,[27] the expected value of inter-sphere distance (d) can be rigorously correlated with the surface density of spheres (n) (Equation (1)). The step-by-step mathematical derivation is presented in the Supporting Information.
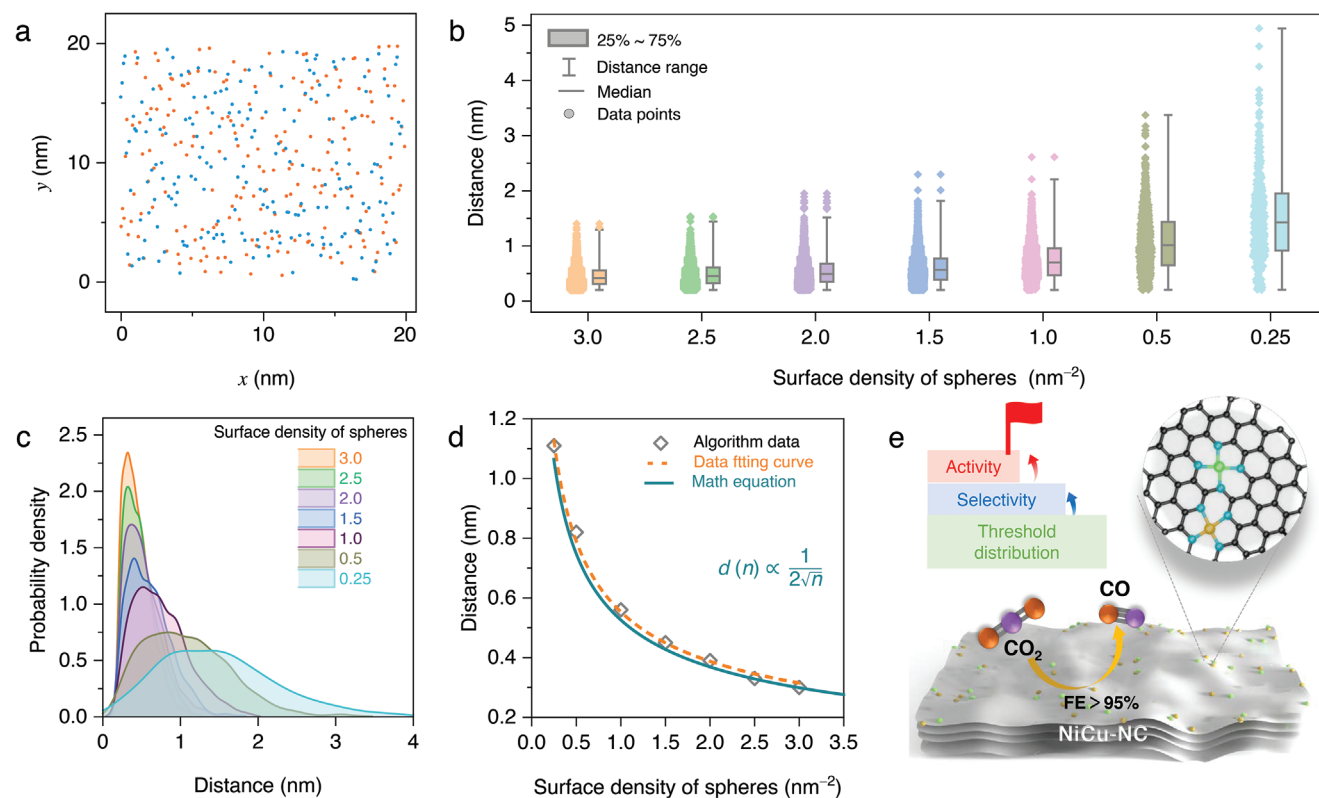

Figure 5. Macro-descriptor of the inter-metal distance for DACs via random distribution analysis. a) The typical position of 400 spheres in two different colors after random distribution on the 20 × 20 nm grid. b) The box-line plot for the statistical illustration of the inter-distance of varied numbers of randomly distributed spheres. c) The probability density curves converted from (b). d) The fitting curve correlating the inter-site distance and the surface density of spheres, based on the mode of distance (peak value) from (c). e) Schematic of Ni and Cu atoms dispersed on multilayered graphene nanosheets within the threshold distance, showing the synergistic effect to boost CRR activity and selectivity.

ADVANCED
SCIENCE NEWS
www.advancedsciencenews.com

ADVANCED
MATERIALS
www.advmat.de

$$d \propto \frac{1}{2\sqrt{n}} \tag{1}$$

It is notable that the fitting curve (orange dash line in Figure 5d) of simulation results shows almost the same coefficient (−0.51) as that from mathematical derivation (−0.5). Considering the experimentally obtained DACs supported on a 2D host substrate (i.e., N-doped graphene, Figure S26, Supporting Information), the d can be further correlated with the intrinsic material parameters (Equation (2)).

$$d \propto (F \times T \times r_a)^{-0.5} \tag{2}$$

where F is a material-dependent factor showing the total atom number of monolayer substrate per unit square, T is the thickness of the 2D substrate, and r_a is the atomic ratio of metal atoms.

Promisingly, such d–r_a correlation can serve as a universal and practicable macro-descriptor to guide the design and synthesis of DACs and SACs with targeted inter-metal distance and favorable performance enhancement by regulating the substrate thickness and metal loading. It has been validated in Fe−N$_4$ SACs for ORR application.[13a] The increase of metal loading will decrease the inter-metal distance of adjacent Fe atoms and optimize the ORR activity. Given the most recent advancement in the SACs formation mechanism[28] and present insight into the d–r_a correlation, the fabrication of well-defined carbonaceous DACs or SACs can be rationally achieved by regulating the carbon precursor amount and type, carbonization method, the vaporization-dependent metal precursor amount, and other related factors. Meanwhile, it is more economic and feasible to synthesize high-performance DACs/SACs with moderate metal loading and threshold inter-metal effect, rather than to pursue ultrahigh metal loading amount (Figure 5e).

3. Conclusion

We have unraveled a critical and qualitative effect of threshold distance between neighboring metals of DACs on the electronic structure and electrocatalytic performance. It has been mutually confirmed by theoretical simulation and experiments, including microscopic, spectroscopic, and electrochemical techniques, as well as computational modelings. By taking NiCu-NC as an example, Ni and Cu atoms featuring a threshold distance of 5.3 Å exhibited non-bonding interaction but the synergistic effect to regulate the electronic structure and promote intermediate adsorption, thus boosting the activity and selectivity of CO_2 electroreduction. The threshold-distributed NiCu-NC DACs exhibited a low onset potential (300 mV) and a wide potential window of ≈800 mV for selective CO_2 electroreduction to CO (>80%), with a maximum FE of ≈98% at −1.07 V versus RHE in 0.1 M KHCO$_3$. The random distribution simulation and mathematical analysis also revealed an effective macro-descriptor to correlate the inter-metal distance with structure features, such as the substrate thickness and metal loading amount. This work stresses the importance of a thorough structural investigation of DACs and paves the way for a deeper understanding of inter-metal interaction with more

rational and realistic principles, which will benefit the design, characterization, and mechanism elucidation of atomically dispersed catalysts in the future.

4. Experimental Section

Experimental details can be found in the Supporting Information.

Supporting Information

Supporting Information is available from the Wiley Online Library or from the author.

Conflict of Interest

The authors declare no conflict of interest.

Data Availability Statement

The data that support the findings of this study are available from the corresponding author upon reasonable request.

Keywords

[1] a) X. F. Yang, A. Wang, B. Qiao, J. Li, J. Liu, T. Zhang, *Acc. Chem. Res.* **2013**, *46*, 1740; b) Y. Chen, S. Ji, C. Chen, Q. Peng, D. Wang, Y. Li, *Joule* **2018**, *2*, 1242; c) C. Tang, Y. Jiao, B. Shi, J. N. Liu, Z. Xie,

X. Chen, Q. Zhang, S. Z. Qiao, *Angew. Chem., Int. Ed.* **2020**, *59*, 9171.

[2] a) K. Liu, J. Fu, Y. Lin, T. Luo, G. Ni, H. Li, Z. Lin, M. Liu, *Nat. Commun.* **2022**, *13*, 2075; b) F. Wu, C. Pan, C.-T. He, Y. Han, W. Ma, H. Wei, W. Ji, W. Chen, J. Mao, P. Yu, D. Wang, L. Mao, Y. Li, *J. Am. Chem. Soc.* **2020**, *142*, 16861; c) Y. Chen, S. Ji, S. Zhao, W. Chen, J. Dong, W.-C. Cheong, R. Shen, X. Wen, L. Zheng, A. I. Rykov, S. Cai, H. Tang, Z. Zhuang, C. Chen, Q. Peng, D. Wang, Y. Li, *Nat. Commun.* **2018**, *9*, 5422; d) F. Zhang, Y. Zhu, C. Tang, Y. Chen, B. Qian, Z. Hu, Y. C. Chang, C. W. Pao, Q. Lin, S. A. Kazemi, Y. Wang, L. Zhang, X. Zhang, H. Wang, *Adv. Funct. Mater.* **2022**, *32*, 2110224.

[3] a) W. Zhang, Y. Chao, W. Zhang, J. Zhou, F. Lv, K. Wang, F. Lin, H. Luo, J. Li, M. Tong, E. Wang, S. Guo, *Adv. Mater.* **2021**, *33*, 2102576; b) J. Zhang, Q.-A. Huang, J. Wang, J. Wang, J. Zhang, Y. Zhao, *Chin. J. Catal.* **2020**, *41*, 783; c) G. Sun, Z. J. Zhao, R. Mu, S. Zha, L. Li, S. Chen, K. Zang, J. Luo, Z. Li, S. C. Purdy, A. J. Kropf, J. T. Miller, L. Zeng, J. Gong, *Nat. Commun.* **2018**, *9*, 4454.

[4] a) F. Calle-Vallejo, D. Loffreda, M. T. M. Koper, P. Sautet, *Nat. Chem.* **2015**, *7*, 403; b) X. Hong, K. Chan, C. Tsai, J. K. Nørskov, *ACS Catal.* **2016**, *6*, 4428; c) Q. Wang, X. Zheng, J. Wu, Y. Wang, D. Wang, Y. Li, *Small Struct.* **2022**, *3*, 2200059.

[5] a) K. P. Kuhl, T. Hatsukade, E. R. Cave, D. N. Abram, J. Kibsgaard, T. F. Jaramillo, *J. Am. Chem. Soc.* **2014**, *136*, 14107; b) H. A. Hansen, J. B. Varley, A. A. Peterson, J. K. Nørskov, *J. Phys. Chem. Lett.* **2013**, *4*, 388.

[6] a) Z. W. Chen, L. X. Chen, C. C. Yang, Q. Jiang, *J. Mater. Chem. A* **2019**, *7*, 3492; b) A. Pedersen, J. Barrio, A. Li, R. Jervis, D. J. L. Brett, M. M. Titirici, I. E. L. Stephens, *Adv. Energy Mater.* **2022**, *12*, 2102715; c) L. Li, K. Yuan, Y. Chen, *Acc. Mater. Res.* **2022**, *3*, 584; d) L. Zhang, R. Si, H. Liu, N. Chen, Q. Wang, K. Adair, Z. Wang, J. Chen, Z. Song, J. Li, M. N. Banis, R. Li, T.-K. Sham, M. Gu, L.-M. Liu, G. A. Botton, X. Sun, *Nat. Commun.* **2019**, *10*, 4936.

[7] a) C. Liu, T. Li, X. Dai, J. Zhao, D. He, G. Li, B. Wang, X. Cui, *J. Am. Chem. Soc.* **2022**, *144*, 4913; b) J. Shan, C. Ye, Y. Jiang, M. Jaroniec, Y. Zheng, S.-Z. Qiao, *Sci. Adv.* **2022**, *8*, eabo0762.

[8] a) L. Jiao, J. Zhu, Y. Zhang, W. Yang, S. Zhou, A. Li, C. Xie, X. Zheng, W. Zhou, S.-H. Yu, H. L. Jiang, *J. Am. Chem. Soc.* **2021**, *143*, 19417; b) Y. Li, W. Shan, M. J. Zachman, M. Wang, S. Hwang, H. Tabassum, J. Yang, X. Yang, S. Karakalos, Z. Feng, G. Wang, G. Wu, *Angew. Chem., Int. Ed.* **2022**, *61*, e202205632; c) X. Zhang, X. Zhu, S. Bo, C. Chen, M. Qiu, X. Wei, N. He, C. Xie, W. Chen, J. Zheng, P. Chen, S. P. Jiang, Y. Li, Q. Liu, S. Wang, *Nat. Commun.* **2022**, *13*, 5337.

[9] Z. Liang, L. Song, M. Sun, B. Huang, Y. Du, *Sci. Adv.* **2021**, *7*, eabl4915.

[10] D. Liu, Y. Zhao, C. Wu, W. Xu, S. Xi, M. Chen, L. Yang, Y. Zhou, Q. He, X. Li, B. Ge, L. Song, J. Jiang, Q. Yan, *Nano Energy* **2022**, *98*, 107296.

[11] Z. Yu, C. Si, A. P. LaGrow, Z. Tai, W. A. Caliebe, A. Tayal, M. J. Sampaio, J. P. S. Sousa, I. Amorim, A. Araujo, L. Meng, J. L. Faria, J. Xu, B. Li, L. Liu, *ACS Catal.* **2022**, *12*, 9397.

[12] Y. Yang, Y. Qian, H. Li, Z. Zhang, Y. Mu, D. Do, B. Zhou, J. Dong, W. Yan, Y. Qin, L. Fang, R. Feng, J. Zhou, P. Zhang, J. Dong, G. Yu, Y. Liu, X. Zhang, X. Fan, *Sci. Adv.* **2020**, *6*, eaba6586.

[13] a) Z. Jin, P. Li, Y. Meng, Z. Fang, D. Xiao, G. Yu, *Nat. Catal.* **2021**, *4*, 615; b) J. Zhu, M. Xiao, D. Ren, R. Gao, X. Liu, Z. Zhang, D. Luo,

W. Xing, D. Su, A. Yu, Z. Chen, *J. Am. Chem. Soc.* **2022**, *144*, 9661; c) H. Li, L. Wang, Y. Dai, Z. Pu, Z. Lao, Y. Chen, M. Wang, X. Zheng, J. Zhu, W. Zhang, R. Si, C. Ma, J. Zeng, *Nat. Nanotechnol.* **2018**, *13*, 411; d) M. O. Cichocka, Z. Liang, D. Feng, S. Back, S. Siahrostami, X. Wang, L. Samperisi, Y. Sun, H. Xu, N. Hedin, H. Zheng, X. Zou, H. C. Zhou, Z. Huang, *J. Am. Chem. Soc.* **2020**, *142*, 15386.

[14] a) T. He, A. R. P. Santiago, Y. Kong, M. A. Ahsan, R. Luque, A. Du, H. Pan, *Small* **2022**, *18*, 2106091; b) W. Li, J. Yang, D. Wang, *Angew. Chem., Int. Ed.* **2022**, *61*, e202213318.

[15] J. Leverett, R. Daiyan, L. Gong, K. Iputera, Z. Tong, J. Qu, Z. Ma, Q. Zhang, S. Cheong, J. Cairney, R. S. Liu, X. Lu, Z. Xia, L. Dai, R. Amal, *ACS Nano* **2021**, *15*, 12006.

[16] Z. Zeng, L. Y. Gan, H. B. Yang, X. Su, J. Gao, W. Liu, H. Matsumoto, J. Gong, J. Zhang, W. Cai, Z. Zhang, Y. Yan, B. Liu, P. Chen, *Nat. Commun.* **2021**, *12*, 4088.

[17] X. Zhi, Y. Jiao, Y. Zheng, A. Vasileff, S.-Z. Qiao, *Nano Energy* **2020**, *71*, 104601.

[18] a) C. Shi, H. A. Hansen, A. C. Lausche, J. K. Nørskov, *Phys. Chem. Chem. Phys.* **2014**, *16*, 4720; b) A. Vasileff, X. Zhi, C. Xu, L. Ge, Y. Jiao, Y. Zheng, S. Z. Qiao, *ACS Catal.* **2019**, *9*, 9411.

[19] a) X. H. Li, S. Kurasch, U. Kaiser, M. Antonietti, *Angew. Chem., Int. Ed.* **2012**, *51*, 9689; b) D. Liu, C. Wu, S. Chen, S. Ding, Y. Xie, C. Wang, T. Wang, Y. A. Haleem, Z. u. Rehman, Y. Sang, Q. Liu, X. Zheng, Y. Wang, B. Ge, H. Xu, L. Song, *Nano Res.* **2018**, *11*, 2217.

[20] C. Xu, A. Vasileff, D. Wang, B. Jin, Y. Zheng, S. Z. Qiao, *Nanoscale Horiz.* **2019**, *4*, 1411.

[21] a) X. Hai, S. Xi, S. Mitchell, K. Harrath, H. Xu, D. F. Akl, D. Kong, J. Li, Z. Li, T. Sun, H. Yang, Y. Cui, C. Su, X. Zhao, J. Li, J. Pérez-Ramírez, J. Lu, *Nat. Nanotechnol.* **2022**, *17*, 174; b) P. Hollins, J. Pritchard, *Surf. Sci.* **1979**, *89*, 486; c) K. S. Smirnov, G. Raseev, *Surf. Sci.* **1997**, *384*, L875.

[22] a) H. Cheng, X. Wu, M. Feng, X. Li, G. Lei, Z. Fan, D. Pan, F. Cui, G. He, *ACS Catal.* **2021**, *11*, 12673; b) L. Jiao, W. Yang, G. Wan, R. Zhang, X. Zheng, H. Zhou, S. H. Yu, H. L. Jiang, *Angew. Chem., Int. Ed.* **2020**, *59*, 20589.

[23] H. Funke, M. Chukalina, A. C. Scheinost, *J. Synchrotron Radiat.* **2007**, *14*, 426.

[24] B. Ravel, M. Newville, *J. Synchrotron Radiat.* **2005**, *12*, 537.

[25] a) K. Krause, C. Lee, J. K. Lee, K. F. Fahy, H. W. Shafaque, P. J. Kim, P. Shrestha, A. Bazylak, *ACS Sustainable Chem. Eng.* **2021**, *9*, 5570; b) Z. Z. Niu, L. P. Chi, R. Liu, Z. Chen, M. R. Gao, *Energy Environ. Sci.* **2021**, *14*, 4169; c) D. M. Weekes, D. A. Salvatore, A. Reyes, A. Huang, C. P. Berlinguette, *Acc. Chem. Res.* **2018**, *51*, 910; d) J. Yang, H. Qi, A. Li, X. Liu, X. Yang, S. Zhang, Q. Zhao, Q. Jiang, Y. Su, L. Zhang, J. F. Li, Z. Q. Tian, W. Liu, A. Wang, T. Zhang, *J. Am. Chem. Soc.* **2022**, *144*, 12062.

[26] a) M. Dunwell, W. Luc, Y. Yan, F. Jiao, B. Xu, *ACS Catal.* **2018**, *8*, 8121; b) C. Xu, X. Zhi, A. Vasileff, D. Wang, B. Jin, Y. Jiao, Y. Zheng, S. Z. Qiao, *Small Struct.* **2021**, *2*, 2000058; c) M. Ma, B. J. Trześniewski, J. Xie, W. A. Smith, *Angew. Chem., Int. Ed.* **2016**, *55*, 9748; d) D. Yao, C. Tang, A. Vasileff, X. Zhi, Y. Jiao, S. Z. Qiao, *Angew. Chem., Int. Ed.* **2021**, *60*, 18178.

[27] G. Marsaglia, B. Narasimhan, A. Zaman, *Commun. Stat. Theory Methods* **1990**, *19*, 4199.

[28] L. Han, H. Cheng, W. Liu, H. Li, P. Ou, R. Lin, H. T. Wang, C. W. Pao, A. R. Head, C. H. Wang, X. Tong, C. J. Sun, W. F. Pong, J. Luo, J. C. Zheng, H. L. Xin, *Nat. Mater.* **2022**, *21*, 681.